PERGAMON

International Journal of Solids and Structures 37 (2000) 2265–2283

INTERNATIONAL JOURNAL OF SOLIDS and STRUCTURES

www.elsevier.com/locate/ijsolstr

Unstable neck formation in a ductile ring subjected to impulsive radial loading

N.J. Sørensen [a,*], L.B. Freund [b]

[a] *Division of Mechanics, Lund University, Box 118, S-22100 Lund, Sweden*
[b] *Division of Engineering, Brown University, Providence, RI 02912, USA*

Received 10 March 1998; received in revised form 2 November 1998

Abstract

Formation and growth of diffuse necks in thin metal rings undergoing high-rate radial expansion under plane strain conditions is studied numerically. The material is described by an elastic–viscoplastic internal variable constitutive relation, so that failure by nucleation and void-growth is taken into account. Adiabatic heating due to plastic dissipation is also incorporated. The influence of imperfections in the form of non-uniform wall thickness and of variations in constitutive parameters is studied. The computations show that long wavelength thickness imperfections gradually increase in amplitude after some initial inelastic deformation but do not result in highly localized neck formation. Instead, a critical, nearly periodic mode with short wavelength appears at rather large overall strain levels. It is from this critical mode that complete ductile failure develops.

1. Introduction

The term 'unstable neck formation' in the present context is meant to emphasize the difference between certain cases of dynamic necking and cases with slow loading relevant for radial expansion and subsequent fragmentation of rings and shells. The famous paper by Mott (1947) containing semi-empirical relations regarding fragment size appears to be one of the first to systematically address the fragmentation process in cylindrical shells. During radial expansion of ductile cylindrical shells or rings, deformation is often found to proceed more or less homogeneously within the plastic range until it is interrupted by the emergence of diffuse necks. It is from these necks that final failure eventually develops. For such structures, an understanding of the role of dynamic necking may be important for a complete description of fragmentation.

* Corresponding author. Fax: +46-46-222-4620.
E-mail address: niels.sorensen@mek.lth.se (N.J. Sørensen).

0020-7683/00/$ - see front matter
PII: S0020-7683(98)00315-1

Under quasistatic plane strain tension, the critical mode for diffuse necking in hypo-elastic rate-independent plastic slabs is the longest wavelength mode. This means that necking is normally initiated at tensile strain levels higher than N where N is the strain hardening exponent for power law hardening materials or in general, that necking occurs shortly after maximum load point has been reached (cf Hill and Hutchinson, 1975). How much higher than this value the critical strain level can be depends on the aspect ratio of the slab; long thin slabs develop a long wavelength diffuse neck at strain levels slightly higher than this value when an imperfection is present that can trigger this first available bifurcation mode. The situation is different for slabs of a hypo-elastic viscoplastic material in that true bifurcation modes are not available at realistic stress levels, but the imperfection sensitivity underlying both rate-independent plastic and slightly viscoplastic material behavior leads to a similar type of diffuse neck when a long wavelength surface imperfection is present. In a material which is slightly rate-sensitive, the critical strain level needed for this type of necking to occur is slightly higher than that found for the corresponding rate-independent case (cf Hutchinson and Neale, 1977).

When the deformation proceeds very rapidly so that material inertia plays a role, necking follows different routes and the formation of one or more necks has been reported for plane strain tension conditions. Necking under dynamic conditions has been studied recently by Knoche and Needleman (1993) for the case of high-rate tension of a round bar. In this study, the size-scale dependence of necking was emphasized and the formation of two necks was demonstrated. Under plane strain conditions necking in planar tensile bars and radially expanding rings was studied by Han and Tvergaard (1995) using rate-independent plasticity. Their study showed that sinusoidal thickness imperfections with long wavelength led to multiple necking, but surface imperfections with shorter wavelength leads to necking at the thin points. Needleman (1991) found that inertia slows down neck development and lowers stress triaxiality in the neck center. An analysis of the bifurcations available for a thin block undergoing constant rapid expansion shows that long wavelength modes are suppressed since their rate of formation is too slow because of inertial resistance (cf Sørensen and Freund, 1997). This analysis also indicates that a general type of unstable necking behavior should be considered for cases with high kinetic energy and/or at high strain.

The present simulations of radially expanding rings may be viewed as a two-dimensional simplification of the Mott problem with radially expanding cylinder shells, so that only a two-dimensional segment of a ring is studied, rather than a three-dimensional cylindrical shell. The focus is on the appearance and development of diffuse necks in a ring segment. The aim is to reveal the common features of dynamic neck formation for the cases studied.

2. Problem formulation and method of analysis

2.1. Field equations

The boundary value problem for a segment of a radially expanding thin ring is analyzed below. The ring is characterized in the undeformed state by mean radius R_0, wall thickness h and the segment has angular extent $\theta_0 = \pi/k$, for integer k. The segment occupies the region $(x^1)^2 + (x^2)^2 = r^2$ with $R_0 - h/2 \leqslant r \leqslant R_0 + h/2$ and $x^2 \cos\theta_0 \leqslant x^1 \sin\theta_0$ relative to a Cartesian coordinate system x^i of material particle labels with origin at the center of the ring. Due to the assumed symmetry, the segment is subject to the following boundary conditions in terms of displacements u_i and nominal tractions T^i referred to the material:

$$u_2 = 0, \quad T^1 = 0 \quad \text{on } x^2 = 0 \tag{1}$$

$$u_1 \sin\theta_0 - u_2 \cos\theta_0 = 0, \quad T^1 \cos\theta_0 + T^2 \sin\theta_0 = 0 \quad \text{on } x^2 \cos\theta_0 = x^1 \sin\theta_0 \tag{2}$$

The balance of momentum is enforced in weak form by means of the principle of virtual work

$$\int_V \tau^{ij}\delta\eta_{ij}\,\mathrm{d}V = \int_s T^i \delta u_i\,\mathrm{d}S + \int_V \rho_0 f^i \delta u_i\,\mathrm{d}V - \int_V \rho_0 \frac{\partial^2 u^i}{\partial t^2}\delta u_i\,\mathrm{d}V \tag{3}$$

Here V and S refer to volume and surface of the material, respectively, in the reference configuration. The covariant components of the Lagrangian strain tensor are denoted η_{ij} and the contravariant components of Kirchhoff stress are denoted by τ^{ij}. The mass density at time $t = 0$ is ρ_0 and δ is the variational operator. The stress and strain tensors in (3) are

$$\tau^{ij} = (\rho_0/\rho)\sigma^{ij}, \quad \eta_{ij} = \frac{1}{2}\left(u_{i,j} + u_{j,i} + u^k_{,i}u_{k,j}\right) \tag{4}$$

with ρ denoting current density and a comma denoting differentiation with respect to position in the reference configuration, and σ^{ij} is Cauchy stress.

2.2. Material model

The material model applied here represents a ductile metal which is described by an elastic–viscoplastic internal variable constitutive equation accounting for failure by void nucleation and subsequent growth (cf Gurson, 1976). The incremental form of the constitutive equation using Cauchy stress σ^{ij} is

$$\hat{\sigma}^{ij} = R^{ijkl}\dot{\eta}_{kl} + \dot{\sigma}^{ij}_0 \tag{5}$$

Here, R^{ijkl} denotes the instantaneous elastic stiffness tensor, $(\dot{\ })$ and $\hat{(\ )}$ denote the material time derivative and the objective derivative in the sense of Jauman, respectively, and $\dot{\sigma}^{ij}_0$ denotes a viscous volume stress rate accounting for viscoplasticity, failure and adiabatic heating effects. The stress rates are related through

$$\dot{\sigma}^{ij} = \hat{\sigma}^{ij} + \left(G^{ik}\sigma^{jl} + G^{jk}\sigma^{il}\right)\dot{\eta}_{kl} \tag{6}$$

The constitutive eqn (5) follows from the elastic constitutive equation

$$\hat{\sigma}^{ij} = R^{ijkl}\left(\dot{\eta}_{kl} - \dot{\eta}^{\mathrm{P}}_{kl} - \dot{\eta}^{\mathrm{T}}_{kl}\right) \tag{7}$$

where the difference between the total strain rate $\dot{\eta}_{kl}$ and the sum of the viscoplastic strain rate $\dot{\eta}^{\mathrm{P}}_{ij}$ and the thermal strain rate $\dot{\eta}^{\mathrm{T}}_{kl}$ is the elastic strain rate, so that (7) is an incremental linear hypo-elastic relation. The moduli in this relation are

$$R^{ijkl} = \frac{E}{1+v}\left[\frac{1}{2}\left(G^{ik}G^{jl} + G^{jk}G^{il}\right) + \frac{v}{1-2v}G^{ij}G^{kl}\right] \tag{8}$$

where the metric tensor in the current configuration has contravariant components G^{ij} and E and v are Young's modulus and Poisson's ratio, respectively. The metric tensor G_{ij} of the current configuration is related to the Lagrangian strain by

$$\eta_{ij} = \frac{1}{2}(G_{ij} - g_{ij}) \tag{9}$$

with g_{ij} denoting the reference configuration metric tensor, so that the density ratio in (4) is

$$\sqrt{\frac{G}{g}} = \frac{\rho_0}{\rho} \tag{10}$$

where the determinants of the metrics in the current and reference configurations are G and g, respectively.

The inelastic material model follows a general framework for internal variable constitutive equations (cf Rice, 1971). The plastic strain rate is taken to follow a relation of the form

$$\dot{\eta}^{\mathrm{P}}_{ij} = \dot{\lambda}\frac{\partial \Phi}{\partial \sigma^{ij}} \tag{11}$$

with λ denoting a plastic multiplier and Φ denoting a potential function which in the present case is of the form

$$\Phi = \frac{\sigma_e^2}{\bar{\sigma}_{\mathrm{f}}} + 2q_1 f \cosh\left(\frac{3q_2\sigma \mathrm{h}}{2\bar{\sigma}_{\mathrm{f}}}\right) - q_1^2 f^{\,2} - 1 = 0 \tag{12}$$

The flow strength (in an average sense) is denoted by $\bar{\sigma}_{\mathrm{f}}$, the Mises stress by σ_{e}, the stress deviator by s^{ij} and the hydrostatic stress by σ_{h}; the definitions are

$$\sigma_e^2 = \frac{3}{2}\sigma^{ij}S_{ij}, \quad s^{ij} = \sigma^{ij} - \sigma_{\mathrm{h}}G^{\,ij}, \quad \sigma_{\mathrm{h}} = \frac{1}{3}\sigma^{i}_{i} \tag{13}$$

The scalar internal variable f in (12) incorporating failure is identified as the 'void volume fraction' since failure in the Gurson model is described in terms of the idealized behavior of spherical voids. Furthermore, the parameters q_1 and q_2 were introduced by Tvergaard (1982), on the basis of numerical results obtained from analyses of void sheets (see also Tvergaard, 1990 for an overview). (Here, $q_1 = 1.25$ and $q_2 = 1.0$). The evolution equation incorporates two effects. The rate of change of void volume fraction is written as the sum of two terms,

$$\dot{f} = \dot{f}_{\mathrm{growth}} + \dot{f}_{\mathrm{nucleation}} \tag{14}$$

where the first term relates to the growth of the spherical voids and the second term addresses the nucleation of new voids at inhomogeneities which are present with the initial volume fraction f_0. Nucleation is assumed to be governed by a strain-level criteria based on a normal distribution with mean strain value ε_{N} and standard deviation s_{N} (cf Chu and Needleman, 1980). The evolution equations for the two contributions in (14) are

$$\dot{f}_{\mathrm{growth}} = (1-f)\dot{\bar{\varepsilon}}^{\mathrm{P}} \tag{15}$$

and

$$\dot{f}_{\mathrm{nucleation}} = \frac{f_0}{s_{\mathrm{N}}\sqrt{2\pi}}\exp\left[-\frac{1}{2}\left(\frac{\bar{\varepsilon}^{\mathrm{P}} - \varepsilon_{\mathrm{N}}}{s_{\mathrm{N}}}\right)^2\right]\dot{\bar{\varepsilon}}^{\mathrm{P}} \tag{16}$$

Here, the matrix average effective plastic strain rate is to be viewed as the average of the effective plastic strain over the matrix part of the material (that is, the part of the material volume not occupied by voids).

From the relation (11) for the viscoplastic flow rule (12), the multiplier $\dot{\lambda}$ is obtained from a balance between plastic work rate $\sigma^{ij}\dot{\eta}^{\mathrm{P}}_{ij}$ and the mean plastic work rate over a reference volume. Only the matrix part contributes to the mean plastic work rate so that

$$\sigma^{ij}\dot{\eta}^{\mathrm{P}}_{ij} = (1-f)\bar{\sigma}_{\mathrm{f}}\dot{\bar{\varepsilon}}^{\mathrm{P}} \tag{17}$$

Thus,

$$\dot{\lambda} = \frac{(1-f)\bar{\sigma}_{\mathrm{f}}\dot{\bar{\varepsilon}}^{\mathrm{P}}}{\sigma^{ij}\dfrac{\partial\Phi}{\partial\sigma^{ij}}} \tag{18}$$

In addition to the balance of momentum, as expressed by (3), the balance of energy must also be enforced. Under the assumption of adiabatic conditions, the energy balance may be approximated by a statement of the form

$$\rho c_{\mathrm{p}}\frac{\partial T}{\partial t} = \chi\tau^{ij}\dot{\eta}^{\mathrm{P}}_{ij} \tag{19}$$

where c_{p} is the heat capacity, T is the temperature, χ is the fraction of plastic work converted to heat and $\dot{\eta}^{\mathrm{P}}_{ij}$ is the viscoplastic strain rate.

An average plastic strain rate is specified to be

$$\dot{\bar{\varepsilon}}^{\mathrm{P}} = \dot{\varepsilon}_0\left(\frac{\bar{\sigma}_{\mathrm{f}}}{g(\bar{\varepsilon}^{\mathrm{P}}, T)}\right)^{1/m} \tag{20}$$

with m denoting the strain rate hardening exponent and g denoting a yield strength of the matrix material at the reference strain rate $\dot{\varepsilon}_0$. The yield strength function is assumed to follow a power law of the form

$$g\left(\bar{\varepsilon}^{\mathrm{P}}, T\right) = \left(\sigma_{01} - \sigma_{02}\exp\left(-\beta T\right)\right)\left(1+\bar{\varepsilon}^{\mathrm{P}}/\varepsilon_0\right)^{\mathrm{N}} \tag{21}$$

with strain hardening exponent N, yield strength parameters σ_{01}, σ_{02} and β, temperature T in $^{\circ}C$ and $\varepsilon_0 = g(0, 20)/E$. Also, to complete the specification of the constitutive model, the thermal strain rate $\dot{\eta}^{\mathrm{T}}_{kl}$ in (7) is given by

$$\dot{\eta}^{\mathrm{T}}_{ij} = \alpha G_{ij}\dot{T} \tag{22}$$

where α is the coefficient of thermal expansion.

2.3. Impulsive loading

The ring is subjected to a radial body force impulse with components $f^{\,i}$

$$f^{\,i} = \begin{cases} F\sin(\pi t/t_0)x^i/r & 0 \leqslant t \leqslant t_0 \\ 0 & t > t_0 \end{cases} \tag{23}$$

where F is the amplitude and t_0 is the duration of the loading.

2.4. Numerical procedure

The numerical method used in the analysis of the boundary value problem is a finite element method based on direct discretization of (3) using quadrilateral elements consisting of four crossed triangles to avoid locking (cf Nagtegaal et al., 1974). Time integration follows an explicit Newmark time integration scheme (cf Belytschko et al., 1976) with lumped mass matrix $\mathbf{M}$ (cf Krieg and Key, 1973). The discretized form of (3) is

$$\mathbf{M}\cdot\ddot{\mathbf{D}} = -\mathbf{F}_1 + \mathbf{F}_2 + \mathbf{F}_3 \tag{24}$$

where $\mathbf{D}$ denotes nodal displacements, the nodal forces $\mathbf{F}_1, \mathbf{F}_2$ and $\mathbf{F}_3$ represent the discretized forms of the internal virtual work term, the surface integral and the volume load integral, respectively, in Eq. (3). The Newmark scheme may be written as

$$\mathbf{D}^{(t+\Delta t)} = \mathbf{D}^{(t)} + \dot{\mathbf{D}}^{(t)}\Delta t + \left[(1/2-k_2)\ddot{\mathbf{D}}^{(t)} + k_2\ddot{\mathbf{D}}^{(t+\Delta t)}\right](\Delta t)^2 \tag{25}$$

$$\ddot{\mathbf{D}}^{(t+\Delta t)} = \mathbf{M}^{(-1)}\cdot\left(\mathbf{F}_2^{(t+\Delta t)} + \mathbf{F}_3{}^{(t+\Delta t)} - \mathbf{F}_1^{(t+\Delta t)}\right) \tag{26}$$

$$\dot{\mathbf{D}}^{(t+\Delta t)} = \dot{\mathbf{D}}^{(t)} + \left[(1-k_1)\ddot{\mathbf{D}}^{(t)} + k_1\ddot{\mathbf{D}}^{(t+\Delta t)}\right]\Delta t \tag{27}$$

The choice $k_2 = 0$ gives an explicit time integration from the state at time t to $t+\Delta t$ without any stiffness matrix computation or iteration. The parameter k_1 is chosen to be $1/2$. Time-stepping starts with updating $\mathbf{D}$, and the $\mathbf{F}$-vectors are computed. The next step is the computation of the nodal accelerations using the lumped (diagonalized) mass matrix and these accelerations are used to update the nodal velocities. The size of the allowed time step is restricted by the smallest element with height d_e, so that

$$\Delta t < \zeta d_e / c_d \tag{28}$$

with c_d denoting the speed of elastic dilatation waves and ζ denoting a constant smaller than unity.

The explicit time integration procedure is combined with a rate-tangent modulus method (cf Peirce et al., 1983) to stabilize the step size in integration of the Gurson model. The rate-tangent modulus method uses a linear interpolation to compute the constitutive quantities somewhere between t and $t+\Delta t$. The effective inelastic strain rate $\dot{\bar{\varepsilon}}^{\mathrm{p}}_*$ used in computing the constitutive quantities is written as

$$\dot{\bar{\varepsilon}}^{\mathrm{P}}_* = (1-\theta_r)\dot{\bar{\varepsilon}}^{\mathrm{P}}(t) + \theta_r\dot{\bar{\varepsilon}}^{\mathrm{P}(t+\Delta t)} \tag{29}$$

where the effective inelastic average strain $\dot{\bar{\varepsilon}}^{\mathrm{P}}(t)$ at time t is computed directly by (20) and $\dot{\bar{\varepsilon}}^{\mathrm{P}(t+\Delta t)}$ may be expressed in terms of the quantities known at time t, the interpolation parameter θ_r and the time step Δt, so that the final form of the constitutive equation is an incremental linear form.

2.5. Thickness imperfections

The surface imperfections are chosen to be sinusoidal variations in wall thickness since interest in the present study is on diffuse necking. The imperfections on the ring segments to be analyzed here are chosen so that they correspond to some of the modes that are first available for bifurcation in the rate-independent, incompressible quasistatic case of plane strain tensile test (cf Hill and Hutchinson, 1975).

The surface imperfections are taken to be thickness variations of the form

$$h = h_0\left[1 - 2\xi \cos\left(n\pi\theta/\theta_0\right)\right] \tag{30}$$

where θ is the angular position around the circumference, h_0 is the initial mean thickness, ξ is the dimensionless imperfection amplitude relative to the half-thickness and n is the integer mode number.

3. Results

For all cases of ring expansion reported here, θ_0 is assumed to be $\pi/8$, implying that one-sixteenth of the full circumference of the ring is considered. This appears to be a sufficiently large sector to demonstrate the unstable necking phenomenon that is the focus of this study. However, within this sector, the influence of variations in geometrical or material parameters is considered. Unless otherwise noted, the material is assumed to be a pressure vessel steel (A533 grade B) which has been thoroughly characterized by Naus et al. (1989). The values of the parameters appearing in the constitutive relations presented above are: $E = 2.069 \times 10^{11}$ Pa, $\nu = 0.3$, $N = 0.1$, $\sigma_{01} = 374.87 \times 10^6$ Pa, $\sigma_{02} = 59.89 \times 10^6$ Pa, $\beta = 0.007933/^\circ$C, $m = 0.002$, $\alpha = 1.1 \times 10^{-5}/^\circ$C, $c_p = 465$ J/kg · K, $f_0 = 0.002$, $\varepsilon_N = 0.3$, $s_N = 0.1$, $\chi = 0.9$ and $\dot{\varepsilon}_0 = 1$ s^{-1}. The initial temperature is $T_0 = 20^\circ$C, the initial density is $\rho_0 = 7850$ kg/m^3, the rate tangent modulus method parameter is chosen to $\theta_r = 0.9$ and the Courant criteria (28) is fulfilled with $\zeta = 0.25$; however, most frequently, the stable step size is set by the rate tangent modulus procedure for integrating the constitutive response. The impulsive loading (23) is specified by the amplitude $F = 10^8$ N/kg and duration $t_0 = 10$ μs. Prior to action of this impulse, the material is stress free and at rest; see Fig. 1. This impulse would result in a radial particle velocity of approximately 637 m/s in the absence of any material resistance. Concerning the initial imperfections in wall thickness, the values $n = 1$ and $\xi = 0.01$ are assumed for each case unless alternate values are given. The finite element mesh used for the computation consisted of a 5×288 array of quadrilaterals, each divided into four triangular elements formed by the diagonals, unless stated to the contrary.

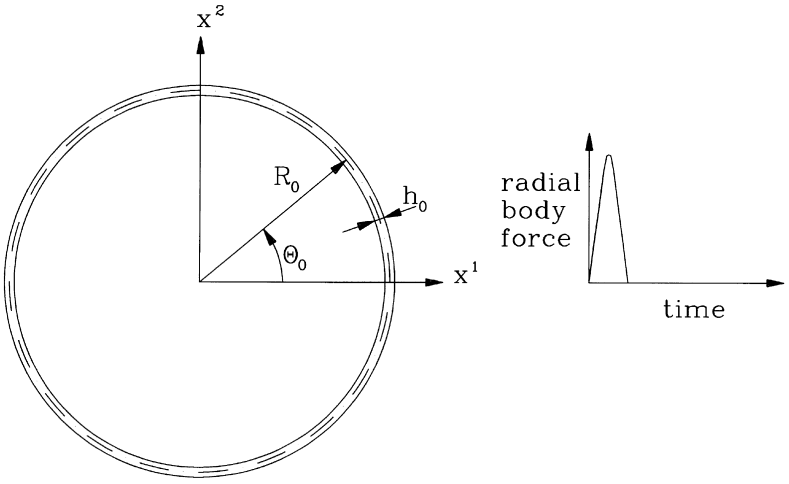

Fig. 1. Schematic drawing illustrating the present impact problem for a thin ring with mean radius R_0 and thickness h. Only a segment of angular dimension $\theta_0 = 22.5^\circ$ is analyzed numerically.

Eight contour plots showing level curves of effective plastic strain after an elapsed time of approximately 100 μs from onset of loading are shown in Fig. 2. In all these cases, the thinner portion of the ring, near $\theta = 0$, is at the right end of the figure. Fig. 2(a) represents the result of the calculation for the default values of the material parameters and other features. For purposes of comparison, the other parts of Fig. 2 indicate the influence of changes in parameters: in Fig. 2(b) the thermal softening has been precluded by setting $\chi = 0$; in Fig. 2(c) the strain hardening exponent is reduced to $N = 0.05$ (from 0.1); in Fig. 2(d) the strain hardening exponent is $N = 0.2$; in Fig. 2(e) the imperfection amplitude is reduced to $\xi = 0.001$ (from 0.01); in Fig. 2(f) a finer mesh consisting of an array of 10×576 quadrilaterals was used (instead of 5×288); in Fig. 2(g) the imperfection mode number is $n = 2$ (instead of $n = 1$); and in Fig. 2(h) the imperfection mode number is $n = 3$.

From this comparison, several qualitative features of behavior are evident. For example, decreasing (2c) or increasing (2d) the hardening exponent N by a factor of two has a significant influence on dynamic necking. On the other hand, thermal softening (2b) seems to play a very minor role in the process. It is noted that the influence of failure by void growth is similar to that of thermal softening, and the results of computation with vanishing density of void-nucleating inhomogeneities $f_0 = 0$ are nearly indistinguishable from those in Fig. 2(a). In general, the fully developed necks in Fig. 2(a)–(d) are at approximately the same sites on the ring, but variations from the default case (2a) obviously exist at a fine scale. The results in Figs. 2(e), (g) and (h) illustrating sensitivity to the parameters used to characterize the imperfection indicate a significant dependence of unstable necking on the surface

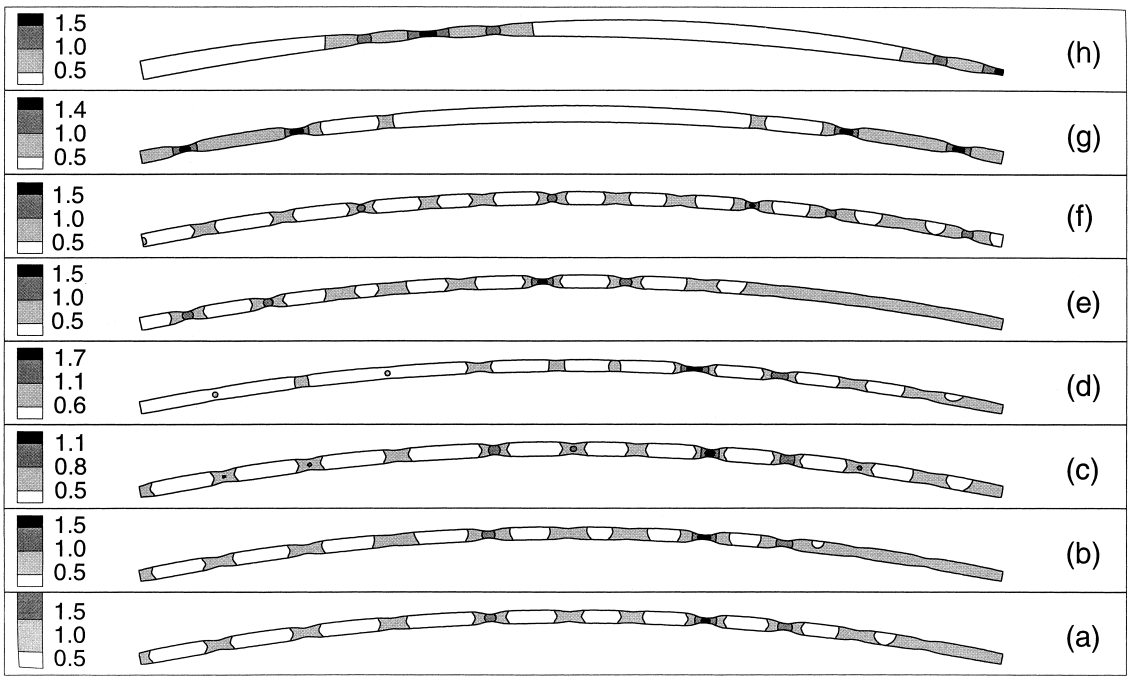

Fig. 2. Contour plot of effective plastic strain ε^{P} showing unstable necks developed in rings with $h_0/R_0 = 1/70$. The angular position varies from $\theta = 0$ at the right end of each ring segment to $\theta = 22.5^\circ$ at the left. (a) Default case based on material parameters for a pressure vessel steel, $\xi = 0.01$, $n = 1$ and 5×288 mesh. The other figures show results obtained by parameter changes from the default case in Fig. 1(a). The parameters changed relative to the case in Fig. 2(a) are: (b) $\chi = 0$ (no heat condition); (c) $N = 0.05$ (reduced hardening); (d) $N = 0.2$ (increased hardening); (e) $\xi = 0.001$, $n = 1$; (f) 10×576 mesh; (g) $n = 2$, $\xi = 0.01$; (h) $n = 3$, $\xi = 0.01$.

imperfection. Although multiple necks developed in each of these cases, the distribution varied strongly with mode number n. Finally, the effect of increasing the mesh resolution (2f) from the default case is to produce a somewhat different neck array, but the salient features are unaltered as described further below.

The results here are all results of high amplitude impulsive loading so that the nominal hoop strain rate is essentially constant, as illustrated in Fig. 3 in the form of graphs of $(R - R_0)/R_0$ vs time t. Of the various parameters which influence the strain rate, strain hardening variations have the largest influence; other parameter variations for the rings with $h_0/R_0 = 1/70$ all result in curves between those for $N = 0.1$ and $N = 0.05$. The average true strain rate $\dot{R}/R$ vs time t is shown in Fig. 4.

In the discussion which follows, a necking process is described as stable if necks form at sites where the wall thickness is minimum and if they grow at rates comparable to the rate of background deformation. On the other hand, a necking process is described as unstable if necks form at sites other than the locations of minimum wall thickness and if they evolve rapidly compared to the rate of background deformation. Some processes involve formation of necks of both types, and these are described as being nearly stable if neither type is clearly predominant.

To explore the evolution of the phenomenon of unstable necking, a normalized strain rate parameter q is introduced. This quantity is defined on the reference midsurface of the ring, and its value is equal to

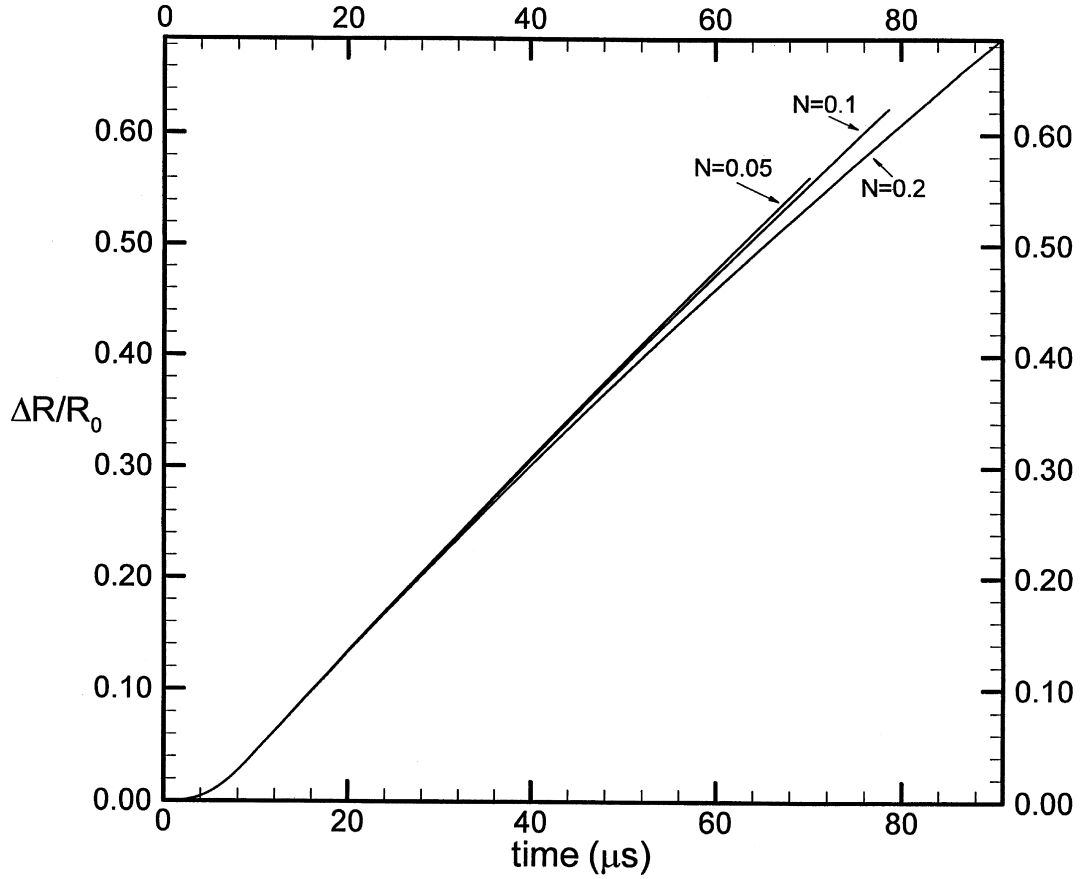

Fig. 3. Average nominal hoop strain $\Delta R/R_0 = (R - R_0)/R_0$ as a function of time for different rings.

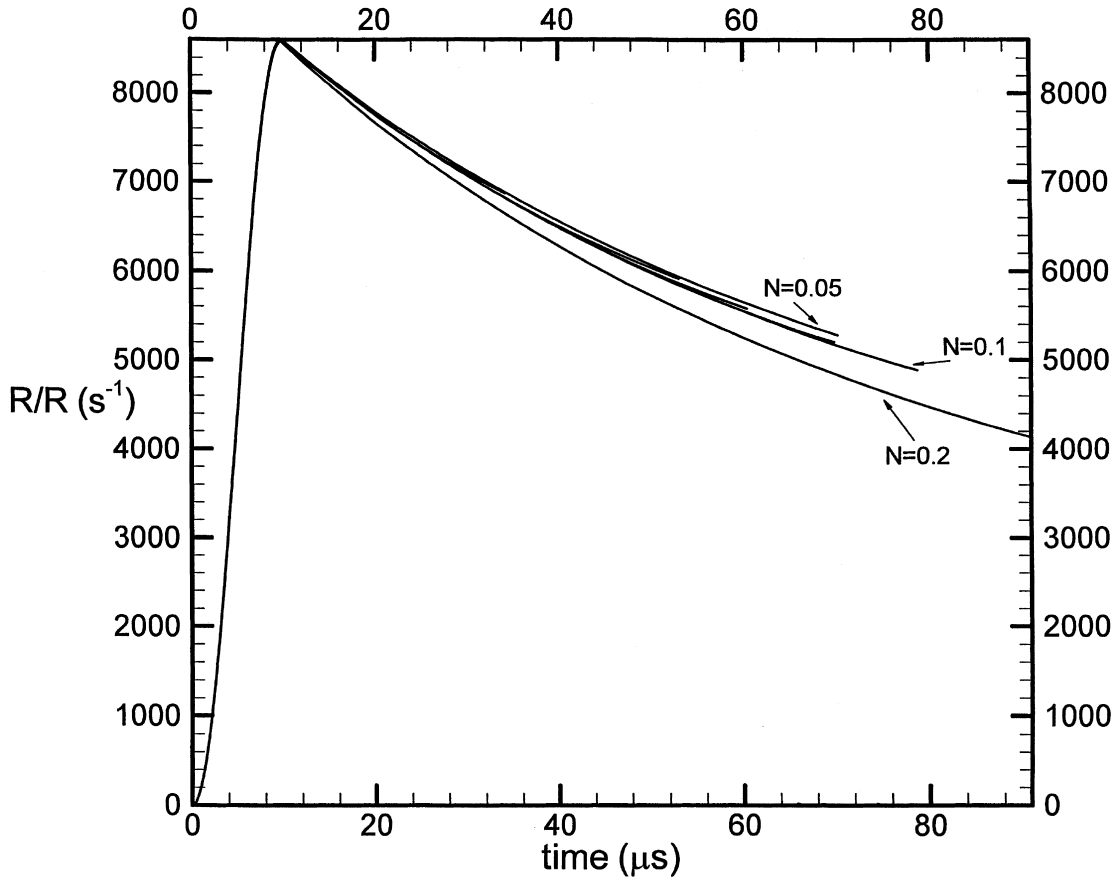

Fig. 4. Average strain rate $\dot{R}/R$ as a function of time for different rings.

the thickness average of the effective inelastic strain rate at that point, normalized by the average background strain rate over the entire solid ($\dot{R}/R$). With this definition, q is a function of initial position θ around the ring and elapsed time t. Thus, the evolution of unstable necks can be observed in a contour plot of $q(\theta, t)$ in the θ, t-plane. Such a plot for the default case is shown in Fig. 5 and features of behavior can be discerned from it. Initially, the deformation is elastic, including some oscillations reflecting non-uniform momentum distribution due to the imperfections present and also including numerical effects resulting from the discretization; much of this portion of the response is excluded from the contour plots in order to focus on the inelastic deformation. As the deformation becomes inelastic, the oscillations are rapidly damped. After an elapsed time of about 20 μs, the plastic strain rate is fairly uniform around the circumference, but slightly larger in the vicinity of the thinner part of the ring. At this point, it appears that a neck will form at the thinner section and that this section will be the eventual failure site.

However, this pattern is perturbed after about 50 μs by the emergence of a localized neck-precursor at about $\theta = 9^\circ$. Within a short time, a cascade of more or less regularly spaced zones of plastic strain localization appear which leads to a global array of neck-precursors; these are the necks evident in Fig. 2(a) at time $t = 79\mu$s. It is noted that the necks are developed to different strain levels in spite of the regularity of the spatial distribution of the neck precursors.

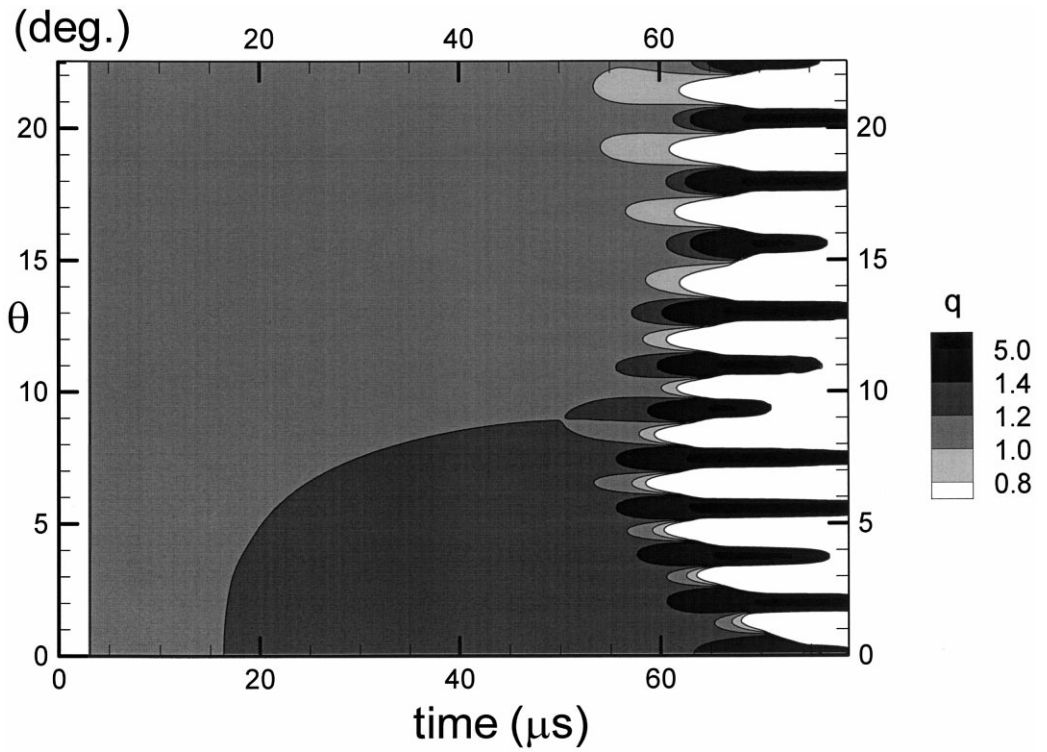

Fig. 5. Neck development in terms of level curves of q, a normalized inelastic strain rate, over the θ, t-plane for case (a) in Fig. 2 (pvs-data, $\xi = 0.01$, $n = 1$ and 5×288 mesh). At the time $t = 7.86 \times 10^{-5}$ s, the deformation state in Fig. 2(a) is reached.

Plots similar to Fig. 5 showing the evolution until the states illustrated in Fig. 2(c)–(f) show the same basic features of an unstable dynamic necking process. Only one additional case is illustrated here, namely the evolution prior to the state in Fig. 2(e) is shown as Fig. 6. The common features among all these processes are that, after some initial elastic oscillations, a non-localized zone of thinning appears (the dark parabola-shaped regions appearing at about $t = 17\ \mu s$ in Figs. 5 and 6) and grows relatively slowly. Later in the deformation, a cascade of localized instabilities appears in the form of a global neck-precursor mode with a nearly constant spacing of localization sites around the circumference. Fully formed necks evolve from some, but not all, of the neck-precursor sites which are evident in Figs. 5 and 6. Within these sites, q is localized within a region of fixed size roughly equal to h in θ but in which q increases rapidly in t.

If all system parameters except the strain hardening exponent N are fixed at the values corresponding to the default case, and the sensitivity of the response to variations in the value of N is probed, then a significant variation in response is observed. If N is varied from 0.05–0.2 (the default value is 0.1), then only small variations in the distribution of necks around the circumference are found. The process of evolution of the neck array is also relatively insensitive to variations in N within this range. However, if N is increased to 0.25, necks are found to develop only in the thinner portion of the ring near $\theta = 0$ (cf Freund and Sørensen, 1997). On the other hand, the spacing of those necks which do form is roughly the same as for the lower values of hardening rate. It should be noted that the features being discussed here are quite coarse over the range of values of q, and more differences between the contour plots for different cases are evident if more closely spaced contour levels are used. Various numerical simulations were carried out to estimate the sensitivity of the contour plots to variations in system parameters. For

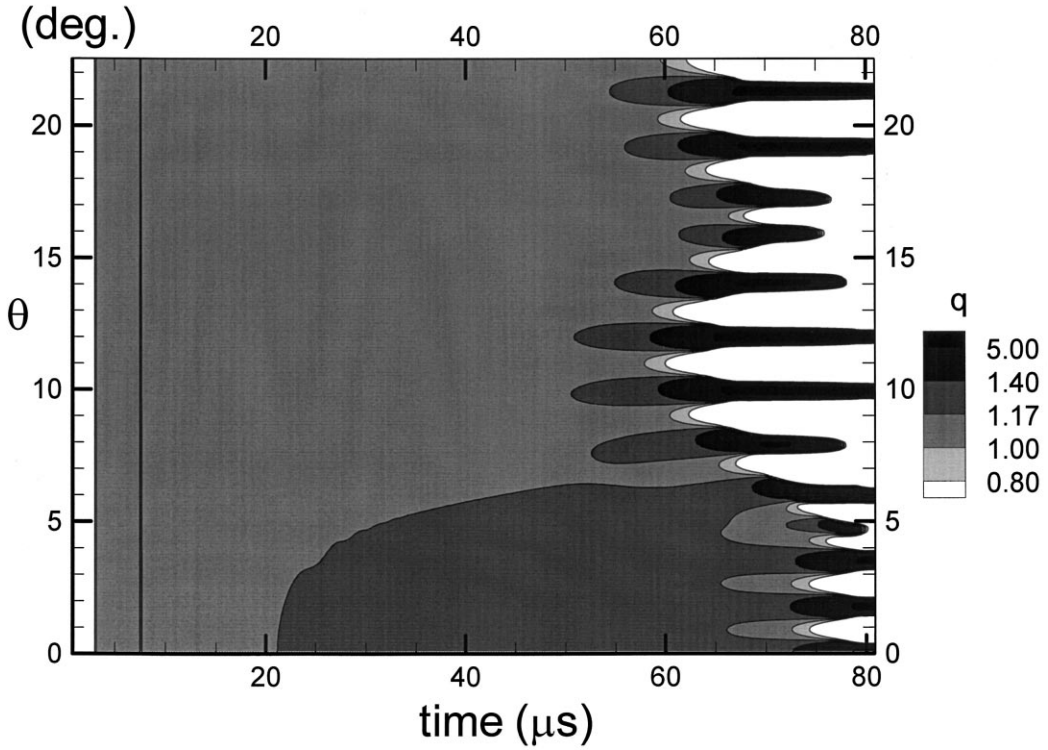

Fig. 6. Contours of constant normalized inelastic strain rate q over the θ, t-plane. End-state corresponds to case (e) in Fig. 2 with $\xi = 0.001$, $n = 1$ (smaller imperfection).

example, a comparison of results obtained with $N = 0.1$ and $N = 0.101$ showed virtually no differences when represented by contour levels of q incremented by 0.02.

It is evident from Fig. 2(e) that the amplitude ξ of the imperfection has an influence on the details of multiple neck formation and, likewise, from Fig. 2(f) that the mesh size has an influence. These features will have to be pursued through systematic parametric studies in order to sort out the details. The important point to be made is that the general features of evolution of a nearly periodic array of closely spaced necks is pervasive in this system over a wide range of system parameters. In all cases where such an array appeared, the spacing between mid-points of the localization zones is approximately 3–4 times h, but with large variation in the degree of thinning within each site.

Somewhat after the first appearance of the neck-precursors, the q-levels drop from $q = 0.8$ to very small levels in the regions between the growing neck-precursors, thus indicating an elastic unloading. The irregularities in the spatial distribution here characterized as unstable necking thus reflect the evolution within short ring-sectors each containing one initially rapid growing neck-precursor surrounded by zones where elastic unloading takes place.

The sensitivity of the results to the imperfection distribution represented by mode number n in (30) is considered by calculating deformation evolution for cases with $n = 2$ and $n = 3$ with all other parameters being held at their default values; the results are shown in Figs. 7 and 8, respectively. As is evident from these figures, the necks in these cases appear in the regions in which the ring wall is initially thinnest. However, multiple closely spaced necks appear in these regions. Furthermore, the growth of these necks seems to correspond to a reduction in strain rate at adjacent points.

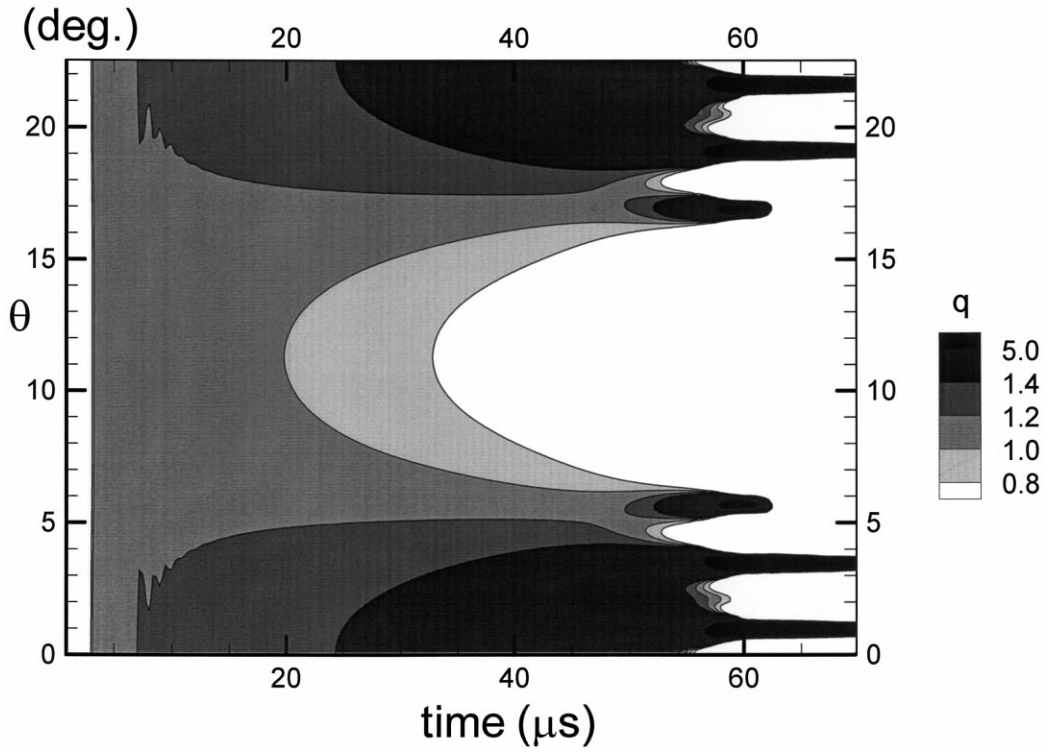

Fig. 7. Contours of constant normalized inelastic strain rate q over the θ, t-plane. The end-state is shown as case (g) in Fig. 1, $n = 2$, $\xi = 0.01$.

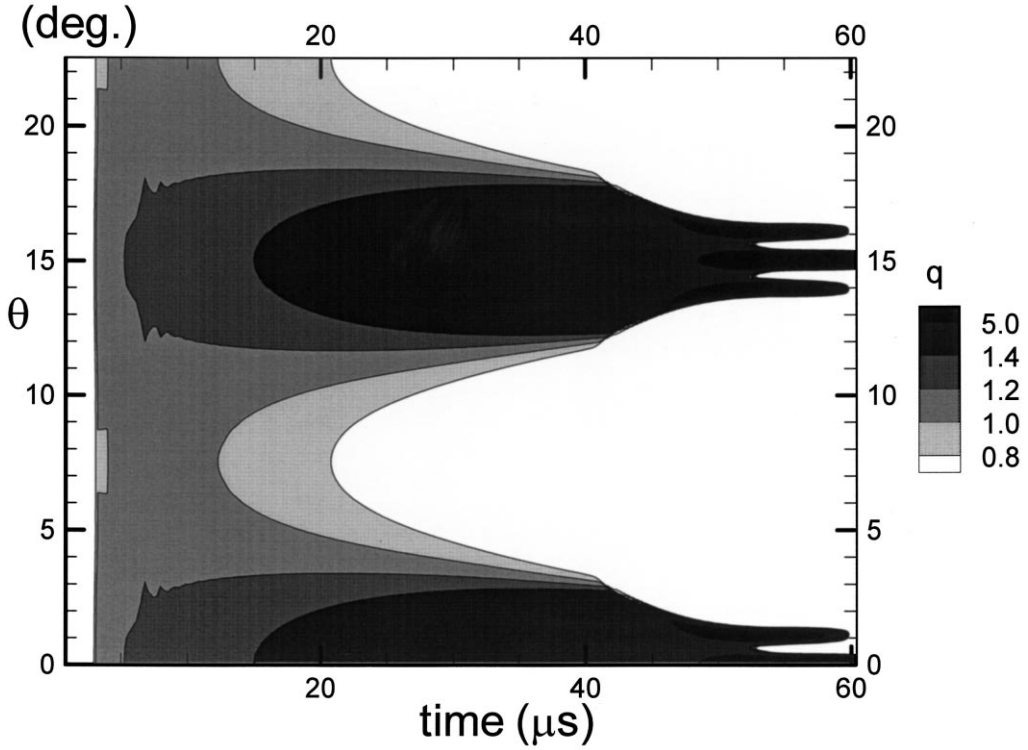

Fig. 8. Contours of constant normalized inelastic strain rate q over the θ, t-plane. The end-state is shown as case (h) in Fig. 1, $n = 3$, $\zeta = 0.01$.

Additional results are shown in Fig. 9 in the form of contour plots of volume fraction f (parts (a), (c) and (f)) and of temperature change (parts (b), (d) and (e)). These cases represent unstable neck formation, nearly stable neck formation and stable neck formation, respectively. Fig. 9(g) shows level curves of void volume fraction for the case when the amplitude of the imperfection is zero ($\zeta = 0$). Finally, Fig. 9(h) is included to provide a direct comparison of a result obtained with the present viscoplastic material model with similar results obtained by Han and Tvergaard (1995) on the basis of a rate-independent plasticity model. When the viscoplastic model was compared with their Fig. 5(d) using $\chi = 0$ and $f = 0$, it was found that $m = 0.001$ gave necking at the same sites as seen in Fig. 9(h), but with some delay in time because the addition of strain rate hardening slows down the ring expansion. With $m = 0.002$ necking occurred at the site of the imperfection. Other parameters used in the comparison are $E = 1.1 \times 10^{11}$ Pa, $N = 1/30$, $\nu = 0.3$, $\sigma_0 = 200 \times 10^6$ Pa, $\rho_0 = 8700$ kg/m^3, $F = 3.45 \times 10^6$ N/kg, $n = 1$ and $\xi = 0.01$.

For the default case (corresponding to Fig. 2(a)), Fig. 9(a) shows clearly that the fourth neck, counting from $\theta = 0$ at the right end of the segment, is the most developed site for ultimate ductile fracture. The companion temperature profile in Fig. 9(b) shows large temperature increases throughout the ring due to plastic dissipation, and particularly high temperatures in the most fully developed necks.

For Fig. 9(c) and its companion Fig. 9(d), the imperfection distribution mode number has been increased to $n = 4$ and, as a result, the process is seen to be nearly stable. Deformation thinning of the wall occurs primarily at those locations where it was initially thinnest. However, at a late stage of the deformation process, these slowly evolving necks abruptly split into closely spaced pairs of unstable necks. Increasing the value of n to integers larger than four always led to stable neck formation. The

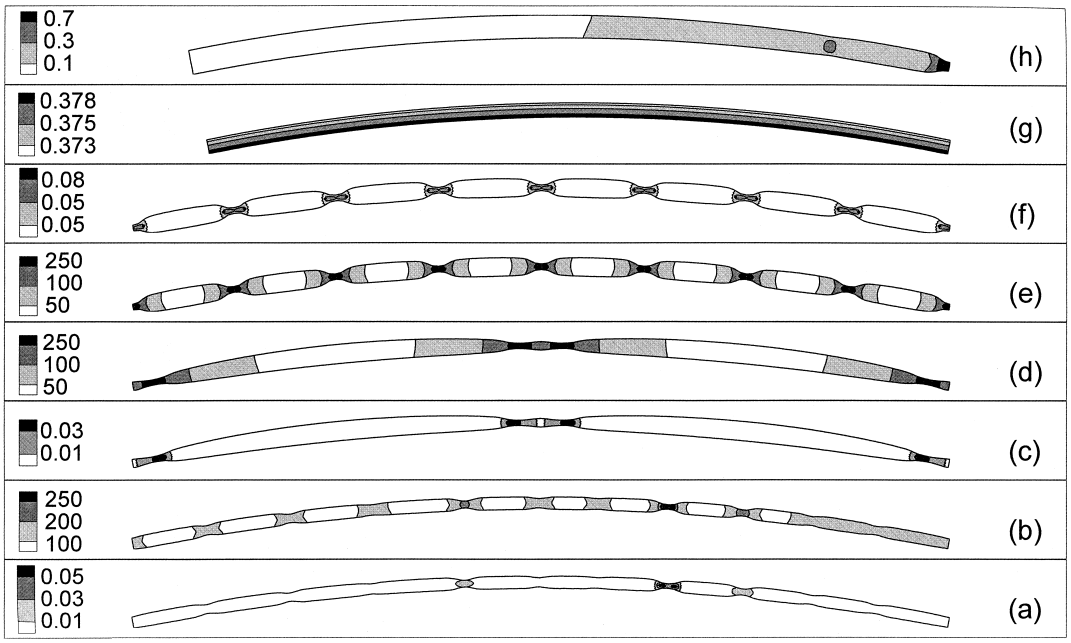

Fig. 9. Contours of constant void volume fraction f (a, c, f) and temperatures (b, d, e) (in °C) for deformed pvs-rings where dynamic necking is unstable (a, b), nearly stable (c, d) and stable (e, f). Initial geometry $h_0/R_0 = 1/70$ in all cases; $n = 1$, $\xi = 0.01$, $t = 7.86 \times 10^{-5}$ s in (a) and (b); $t = 5.29 \times 10^{-5}$ s, $n = 1$, $\xi = 0.01$ in (c) and (d); $t = 5.14 \times 10^{-5}$ s, $n = 16$, $\xi = 0.001$ in (e) and (f). The angular dimension $\theta = 0°$ at the right of the figures and $\theta = \theta_0 = 22.5°$ at the left. In (g) no imperfection ($\xi = 0.01$) is present ($t = 4.99 \times 10^{-5}$ s). In (h) data from Han and Tvergaard (1995) were used, $n = 1$, $\xi = 0.01$ and $t = 14.2 \times 10^{-5}$ s.

case with $n = 16$ and $\xi = 0.001$ is illustrated in Fig. 9(e) and (f). It is seen that virtually identical necks form at each location around the circumference at which the wall was initially thinnest due to the small imperfection. This example also demonstrates the capability of the computational procedure to follow a stable deformation far into the large strain regime.

Fig. 9(g) shows the contour plot of void volume fraction f at a value of hoop strain of $\Delta R/R_0 = 0.375$ for the case when the amplitude of the imperfection distribution is $\xi = 0$. Evidently, the deformation has remained uniform up to the mean strain of 0.375. With a very small imperfection of $\xi = 10^{-6}$, necks first appeared at average hoop strains $\Delta R/R_0$ in the range from 0.45–0.5. With higher strain rate hardening (that is, higher values of m) and higher strain hardening (higher values of N), necking was delayed to higher strain levels; for $\xi = 0$, no visible necks had yet appeared at a value of $\Delta R/R_0$ close to unity with $m = 0.01$ and $N = 0.25$.

The deformation history for two cases with stable necking (or nearly stable necking) are shown in the form of contour plots of normalized average inelastic strain rate q in Figs. 10 and 11. The end state for the case in Fig. 10 corresponds to the plots in Figs. 9(c) and (d), for which $n = 4$ and $\xi = 0.01$. The splitting of the neck-precursors into two separate necks is seen to occur at a very late time so that necking is nearly stable in this case. The surface imperfections represented by $n = 8$, $\xi = 0.01$ and $n = 16$, $\xi = 0.001$ both lead to completely stable necking; the former case is illustrated in Fig. 11. The zones of higher-than-average plastic strain rate (Fig. 11) show that necking becomes gradually more localized with time, but an abrupt localization appears around 27 μs. The common feature for the deformation history plots in Figs. 10 and 11 is that neck development is initiated at the points around the

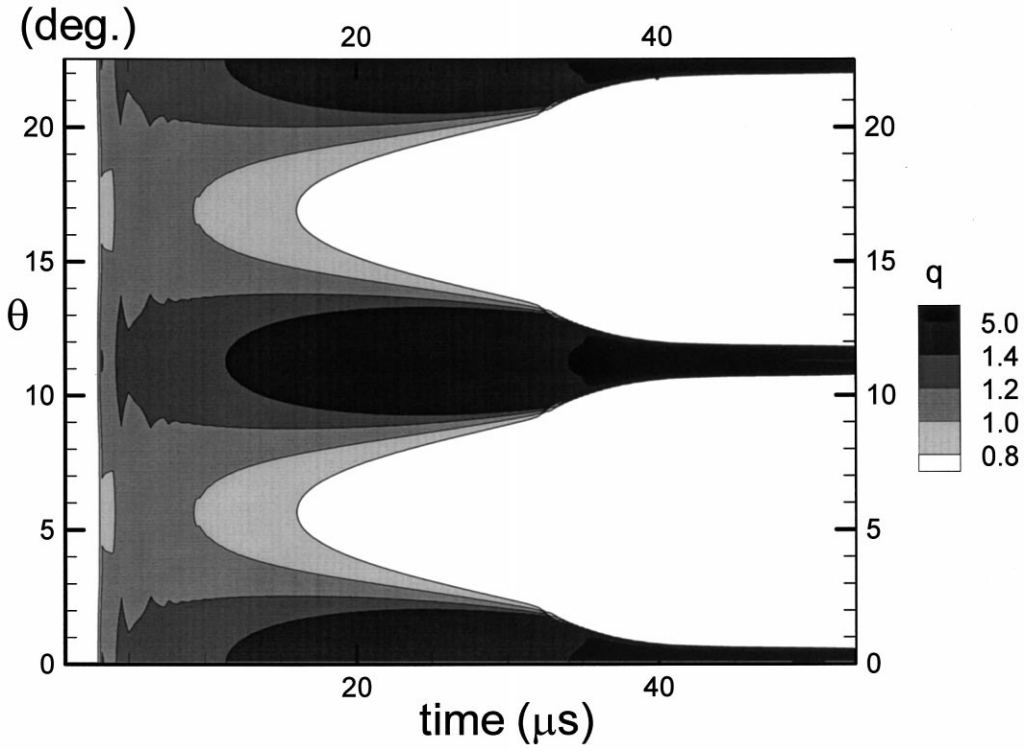

Fig. 10. Contours of constant normalized inelastic strain rate q over the θ, t-plane. Nearly stable neck development for the case $n = 4$, $\xi = 0.01$. The end-state corresponds to cases (c) and (d) in Fig. 9.

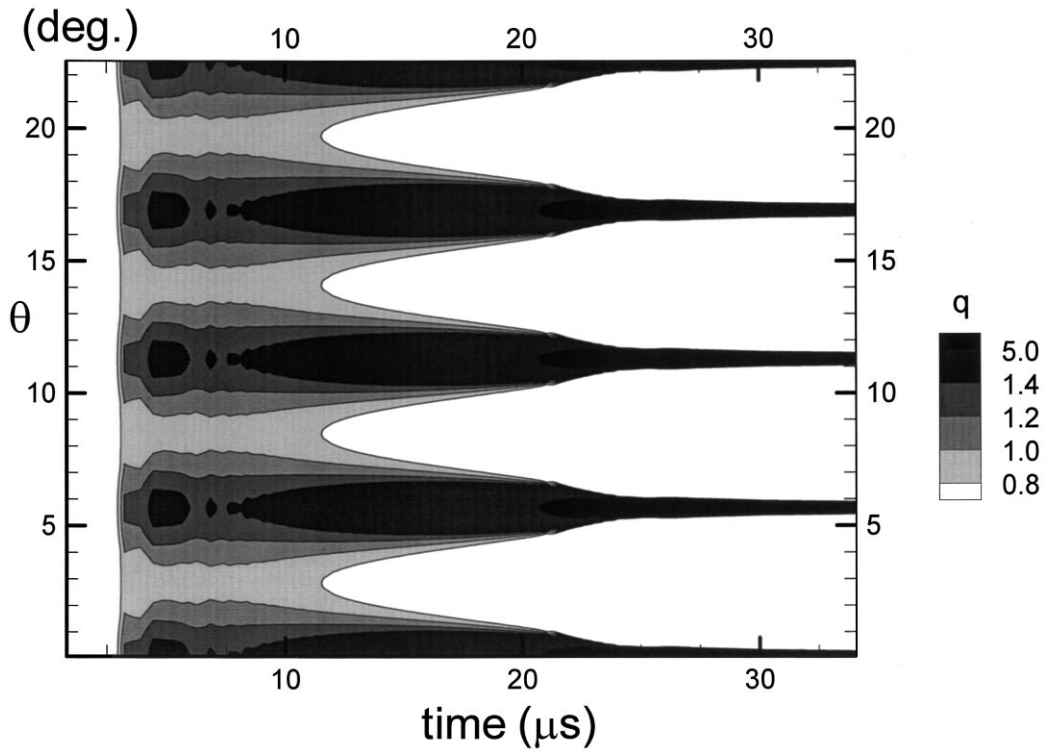

Fig. 11. Contours of constant normalized inelastic strain rate q over the θ, t-plane. Stable neck development; $n = 8$, $\xi = 0.01$.

circumference at which the wall is initially thinnest. The case with $n = 16$ and $\xi = 0.001$ gave results qualitatively identical to those in Fig. 11 where $n = 8$ and $\xi = 0.01$ and very similar to the case with $n = 16$, $\xi = 0.01$, so that the combination of small imperfection size and high mode number is sufficient to trigger a stable type of localization.

The effect of variation in wall thickness is very significant in establishing the number of neck-precursor, as shown in Figs. 12 and 13 for the cases of a thicker ($h_0/R_0 = 1/35$) and a thinner ($h_0/R_0 = 1/140$) ring, both with $n = 1$ and $\xi = 0.01$. The thinner ring has 20 visible neck-precursors, the thicker ring has only 7.5; these numbers are compared with the default case in Fig. 2 ($h_0/R_0 = 1/70$) which has 12.5. In general, the cases with thicker and the thinner rings show the same basic features for the unstable necks reported above, namely, indication of a convective instability (i.e. gradual thinning) at the site of the long wavelength imperfection ($n = 1$, $\xi = 0.01$) and a nearly periodic critical mode, but irregular distribution of the necks which ultimately grow into ductile fractures.

4. Conclusions

Neck formation in rings subjected to a radial impulse of short duration was found to occur mainly by either of two mechanisms, depending on the details of a continuous, periodic imperfection in wall thickness and on material parameters. For lack of a better terminology, the mechanisms are termed stable and unstable, and the essential qualities can be described in the following way. For a given imperfection in wall thickness, a necking process is termed stable if necks evolve only from those sites

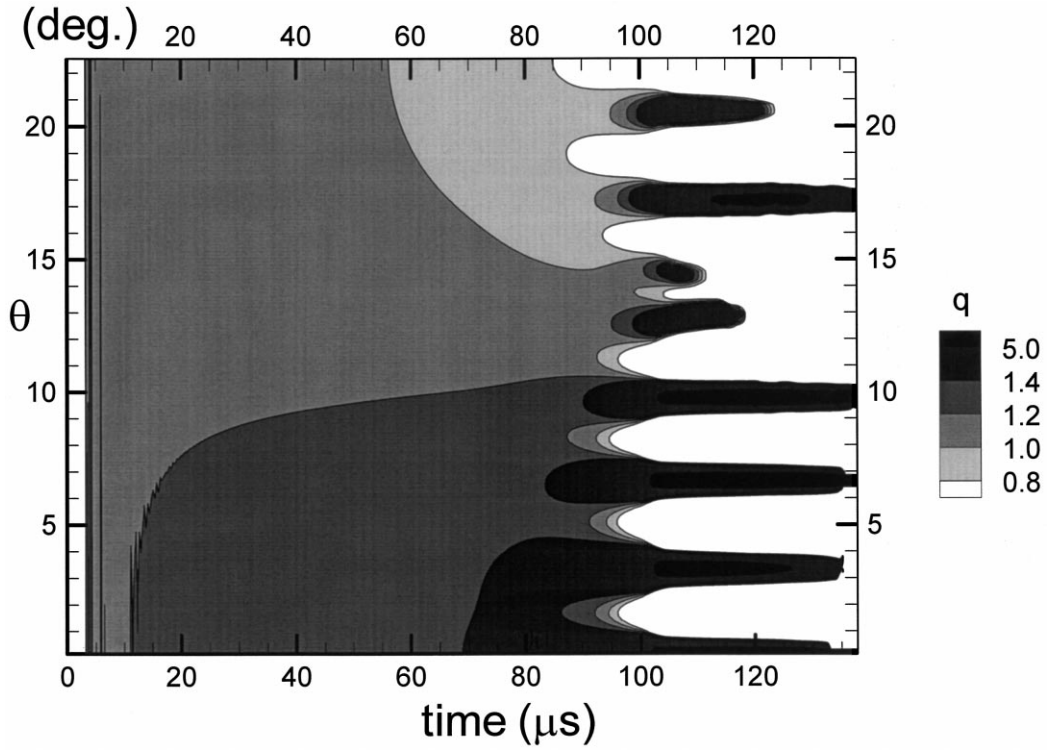

Fig. 12. Unstable neck development in thick ring ($h/R_0 = 1/35$) represented by contours of constant q-values over the θ, t-plane; $n = 1$, $\xi = 0.01$

around the circumference at which the wall thickness is initially minimum. This is the kind of behavior expected if a ring is expanded under slow loading conditions. Nearly all cases of ring expansion show a tendency toward stable neck formation in the early stages of plastic deformation. However, in cases with long wavelength imperfections, the tendency toward stable (in this sense) necking gave rise to mean inelastic strain rates at these sites only slightly higher than the back-ground rates, thus indicating that the background velocity is too large to allow for neck-formation at these sites. This means that the imperfection sensitivity of the material is suppressed by the background motion for these cases. Instead the slow thinning that follows from these imperfections was interrupted in the later stages of plastic deformation by the appearance of multiple necks with more or less regular spacing and which grew relatively rapidly. The locations of these necks correlated only weakly, and in some cases not at all, with the imperfection distribution. The necking process leading to formation of such necks is termed unstable. The general observations are summarized below on the basis of this distinction.

For the impulse parameters used in the present investigation, stable neck formation was found to occur for cases with a relatively large mode number n in the imperfection distribution. For the case studied most thoroughly, with $h_0/R_0 = 1/70$ and $\xi = 0.01$, this was the predominant response mode for $n \geqslant 4$.

In cases with an imperfection with long wavelength ($n < 4$) and/or with small amplitude ($\xi \leqslant 0.01$), an array of more or less regularly spaced neck-precursors appeared around the circumference of the ring relatively late in the process. The spacing of the necks in the array appeared to have little correlation with the initial imperfection distribution in the wall. The irregularities in the spatial distribution

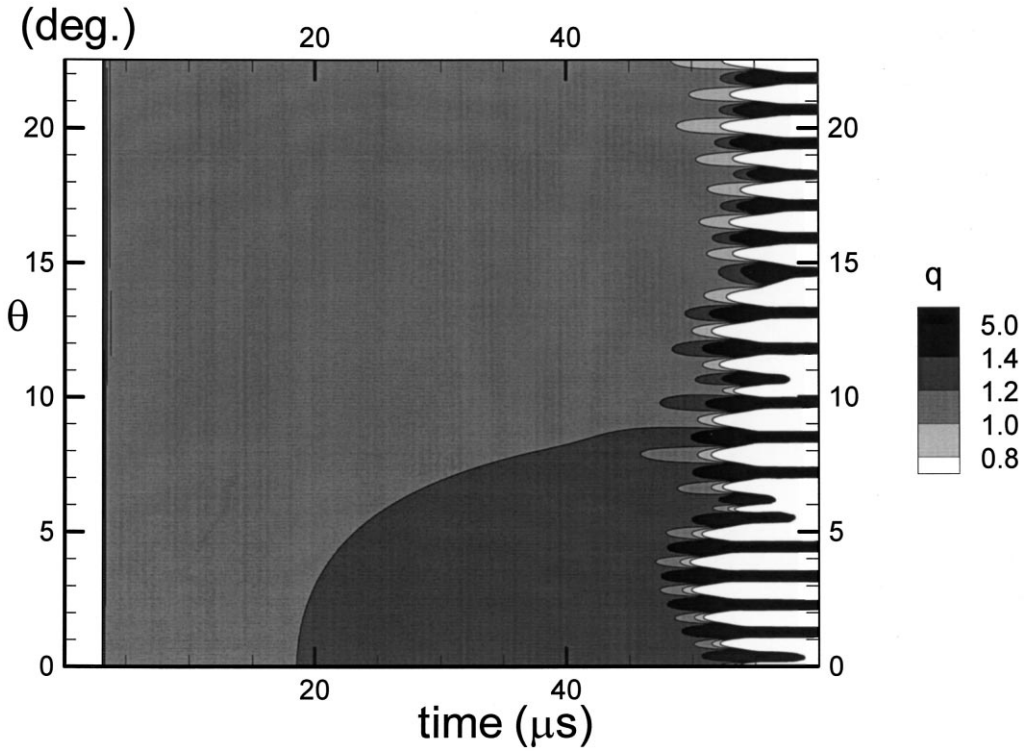

Fig. 13. Unstable neck development in thin ring ($h/R_0 = 1/40$) represented by contours of constant q-values over the θ, t-plane; $n = 1$, $\xi = 0.01$.

characteristic for unstable necking occurred when elastic unloading zones had developed around a neck-precursor.

In cases where unstable neck formation occurred, the spacing of the individual neck-precursors was about $3-4h$. This feature was surprisingly insensitive to variations in material properties, except that the appearance of this mode in some segments of the ring could be suppressed by making the strain hardening parameter N greater than about 0.2.

Both plastic strain rate sensitivity and plastic strain dilation seemed to have only a minor influence on development of unstable necks in this process.

There are far too many parameters in this system to permit a full parametric study of the connection between parameter values and response mode. However, the present results are sufficient to establish a mode of ductile fracture in materials subjected to rapid loading. It is intended to pursue the phenomena introduced here through case studies motivated by particular physical systems.

Acknowledgements

The research support of the Basic Engineering Sciences Division, U.S. Department of Energy, Grant No. DE-FG02-95ER14561, is gratefully acknowledged. The authors are pleased to acknowledge helpful discussions with Prof. Alan Needleman of Brown University. Niels J. Sørensen is grateful for the hospitality and support from the Division of Engineering at Brown University, during a research visit.

References

Belytschko, T., Chiapetta, R.L., Bartel, H.D., 1976. Efficient large scale non-linear transient analysis by finite elements. International Journal of Numerical Methods in Engineering 10, 71–84.

Chu, C.C., Needleman, A., 1980. Void nucleation effects in biaxially stretched thin sheets. Journal of Engineering Materials and Technology 102, 249–256.

Freund, L.B., Sørensen, N.J, 1997. Unstable neck formation as a precursor to ductile fracture during high-rate planar extension. In: Karihaloo, B., Mai, Y., Ripley, M., Ritchie, R.O. (Eds.), Advances in Fracture Research, vol. 6. Pergamon Press, Oxford, pp. 2685–2696.

Gurson, A.L., 1977. Continuum theory of ductile rupture by void nucleation and growth—Part I. Yield criteria and flow rules for porous ductile media. J. Eng. Matr. Tech. 99, 2–15.

Han, J., Tvergaard, V., 1995. Effect of inertia on the necking behavior of ring specimens under rapid radial expansion. Europ. J. Mech. A/Solids 14, 287–307.

Hill, R., Hutchinson, J.W., 1975. Bifurcation phenomena in the plane strain tensile test. J. Mech. Phys. Solis. 23, 239–264.

Hutchinson, J.W., Neale, K.W., 1977. Influence of strain rate sensitivity on necking under uniaxial tension. Acta Met. 25, 839–846.

Knoche, P., Needleman, A., 1993. The effect of size on ductility of dynamically loaded tensile bars. Europ. J. Mech. A/Solids 12, 585–601.

Krieg, R.D., Key, S.W., 1973. Transient shell response by numerical time integration. International Journal of Numerical Methods in Engineering 7, 273–286.

Mott, N.F., 1947. Fragmentation of shell cases. In: Proc. Royal Soc. of London, Series A, 189, pp. 300–308.

Nachtegaal, J., Parks, D.M., Rice, J.R., 1974. On the numerical accurate finite element solutions in the fully plastic range. Computer Method in Applied Mechanics and Engineering 4, 153–177.

Naus, D.J., Keeney-Walker, J., Bass, B.R., Fields, R.J., De Wit, R., Low III, S.R., 1989. High-temperature crack-arrest behavior in 152-mm-thick SEN wide plates of quenched and tempered A533 grade B class 1 steel, NUREG/CR-5330 (ORNL/TM-11083). Oak Ridge National Laboratory, National Institute of Standards and Technology.

Needleman, A., 1991. The effect of inertia on neck development. In: Young, W.H. (Ed.), Topics in Plasticity. AM Press, Ann Arbor, MI, pp. 151–160.

Peirce, D., Shih, C.F., Needleman, A., 1984. A tangent modulus method for rate dependent solids. Computers and Structures 18, 875–887.

Rice, J.R., 1971. Inelastic constitutive relations for solids: an internal-variable theory and its application to metal plasticity. J. Mech. Phys. Solids 19, 433–455.

Sørensen, N.J., Freund, L.B., 1998. Dynamic bifurcation during high-rate planar extension of a rectangular block. Eur. J. Mech. Solids 17, 709–724.

Tvergaard, V., 1982. Ductile failure by cavity nucleation between larger voids. J. Mech. Phys. Solids 30, 265–286.

Tvergaard, V., 1990. Material failure by void growth to coalescence. In: Hutchinson, J.W., Wu, T. (Eds.), Advances in Applied Mechanics, vol. 27. Academic Press, New York, pp. 83–151.